Materials Research. 2022; 25:e20210594
DOI: https://doi.org/10.1590/1980-5373-MR-2021-0594

Oxide Formation in a Melt Spun Alloy in the Zr-Ni-Cu System

***Nelson Delfino de Campos Neto*[a,b*], *Leonardo Pratavieira Deo*[c], *Marcio Andreato Batista Mendes*[d], *Michael Joseph Kaufman*[b], *Marcelo Falcão de Oliveira*[a]**

[a]*Universidade de São Paulo, Escola de Engenharia de São Carlos, Departamento de Engenharia de Materiais, São Carlos, SP, Brasil.*

[b]*Colorado School of Mines, George S. Ansell Department of Metallurgical and Materials Engineering, 1500 Illinois St., Golden, CO 80401, USA.*

[c]*Universidade Federal de Lavras, Departamento de Engenharia, Lavras, MG, Brasil.*

[d]*Universidade Tecnológica Federal do Paraná, Departamento de Engenharia de Materiais, Londrina, PR, Brasil.*

Received: November 22, 2021; Revised: April 2, 2022; Accepted: May 5, 2022

The microstructure of a melt-spun $Zr_{28}Ni_{44}Cu_{28}$ (at. %) alloy was characterized in order to determine the structures and compositions of the crystalline phases that compete with glass formation during rapid solidification. Two crystalline phases were identified, namely, a face centered cubic (FCC) zirconium oxide phase and a primitive cubic version of the big-cube oxide phase, using a combination of scanning electron microscopy, energy dispersive X-ray spectroscopy, X-ray diffraction, and transmission electron microscopy techniques. Our results indicate that the Zr-O atomic pair interaction is preferential compared to the other atomic pair possibilities, supporting the formation of Zr-based oxides over the equilibrium phases in the ternary Zr-Ni-Cu system. Further, the results provide insight into the mechanisms of oxygen-induced crystallization in Zr-based BMGs and the corresponding decrease in glass forming ability (GFA) with increasing oxygen concentrations.

Keywords: *Metallic glass, Zr-Ni-Cu system, zirconium oxide, big-cube.*

1. Introduction

Since the 1960s the rapid solidification techniques are broadly used to produce metallic glasses which have attracted scientific and commercial attention because of their unique physical and mechanical properties[1]. Examples of these properties include their large elastic deformation, high fracture strength, low modulus and good corrosion resistance[2-4]. These unique properties are the consequence of the atomic structure which has no long-range order and no grain boundaries and crystal defects.

Metallic glass forming alloys containing large amounts of zirconium have been studied most extensively, in which Cu and Ni are two important alloying additions[5] where it has been shown that bulk metallic glasses (BMGs) can be produced over a wide composition range in the Zr-Cu binary system with thicknesses up to 2 mm[6]. Consequently, this system is the baseline for many metallic glasses considered promising as engineering materials[7].

In addition, Ni-based BMGs have been successively developed in the past three decades. These Ni-based alloys usually exhibit high thermal stability, good mechanical properties and excellent corrosion resistance[8]. For example, the plastic region to failure and fracture strength of $Ni_{59}Zr_{16}Ti_{13}Si_3Sn_2Nb_7$ BMG can exceed 6.5% and 3 GPa, respectively[9]. The corrosion rate of a $(Ni_{60}Nb_{10}Ta_{30})_{0.95}P_5$ BMG during immersion in HCl is almost zero[10].

The combination of somewhat superior properties and lower material cost has led investigators to further investigate Ni-based BMGs as engineering materials. The maximum critical size that can be achieved for Ni–based BMGs is ~3 mm in the Ni–Nb–Ti–Zr–Co and Ni–Nb–Sn systems and 5 mm in Ni–Zr-based BMGs in the Ni–Zr–Ti–Si–Sn–Nb and Ni–Zr–Ti–Al–Cu systems[11].

It has been shown that alloys with high glass forming ability (GFA) usually are multi-component where the components tend to have both high negative enthalpies of mixing and large atomic size differences[5]. According to these conditions, a selection criterion was developed in our previous work[12] and applied to the Zr-Ni-Cu ternary system in order to identify the alloy compositions with high GFAs, and a good agreement between calculated and experimental results was reported; however, some discrepancies were also observed. The main reason for these discrepancies was attributed to contamination with oxygen during the solidification process, given that oxygen is known to affect the crystallization behavior, as well as, the GFA of undercooled alloys with large amount of zirconium[13].

Oxygen is a common contaminant in the zirconium used in Zr-containing alloys or it is picked up during the melting and casting process. Thus, melting of alloys is usually performed in a Ti-gettered argon atmosphere; however, there is likely always some residual oxygen in the melting chamber[14]. The oxygen contamination is known to change the crystal nucleation kinetics dramatically, triggering the formation

*e-mail: ndelfino@mines.edu

of crystalline phases and these phases may deteriorate the glass-forming ability of the BMG. Specifically, these oxides act as heterogeneous nuclei for the growth of other stable and metastable crystalline phases, which compete against the glass formation[15].

In this context, the present work presents the characterization of melt-spun crystalline microstructures developed at high cooling rates for a $Zr_{28}Ni_{44}Cu_{28}$ (at.%) alloy. We have reported in our previous study that melt-spun ribbons of this alloy consist of both glassy and crystalline phases when contaminated with a relatively high oxygen concentration (e.g., ~700 wppm)[12]. A zirconium oxide and a primitive big-cube phase were identified as the crystalline phases in these ribbons and, to our knowledge, there are no reports in the literature about the characterization of these phases under this specific solidification condition in alloys from the Zr-Ni-Cu system. Therefore, the present study was conducted in an effort to obtain a better understanding of the mechanisms of oxygen-induced crystallization during rapid solidification of Zr-Ni-Cu BMGs as well as an understanding of the GFA decrease due to oxygen contamination in these alloys.

2. Materials and Methods

High purity (99%+) zirconium, nickel, and copper were melted and mixed using non-consumable arc melting to produce a 6 g ingot of a $Zr_{28}Ni_{44}Cu_{28}$ (at.%) alloy. Small sections of the ingots were then used to produce ribbons by melt spinning according to a procedure described in detail in our previous work[12]. The cooling rate during the melt-spinning varies from 10^5 to 10^6 K/s[16,17], and produces a 30-50 μm ribbon thickness that is 3-4 mm in width.

The ribbon was cut into sections ~10 mm in length and subsequently mounted on aluminum stubs using conductive carbon tape for the SEM surface analysis. Cross-sections of the ribbons were cold mounted for similar analysis, after standard metallographic grinding and polishing procedures. SEM was performed using a FEI Quanta 600i SEM with a tungsten source with 20 kV accelerating voltage coupled with an EDS detector. Secondary electron imaging (SEI) was used to analyze the ribbon surface, while backscattered electron imaging (BSE) was used to analyze the ribbon cross-sections. Finally, EDS was used to measure the compositions of the different regions observed in the SEM.

XRD analysis of the ribbon surfaces was performed using a Phillips X'pert diffractometer operating at 45 kV and 40 mA using Cu K_α ($\lambda = 1.5418$ Å) radiation with a step time of 1 s and a step size of 0.02° under 2Θ scans from 25° to 90° for phase identification. Differential scanning calorimetry (DSC) of the ribbons was performed using a Netszch DSC 404 at 20ºC/min heating rate to evaluate the thermal parameters of the amorphous structure.

Disks 3 mm in diameter were cut from the ribbons for TEM analysis, first being thinned to a central perforation (hole) using a dual jet electropolisher (E. A. Fischione and Struers). A polishing solution of 90 vol% ethanol and 10 vol% HNO_3 was used, operating at -20 °C with an applied voltage of 6 V and current between 25 and 30 mA. TEM analysis was performed using a Philips CM12 transmission electron microscope with a tungsten filament and an acceleration voltage of 120 kV. The microstructural characteristics of the investigated alloy were examined using bright field (BF) images and selected area electron diffraction (SAED) was used to confirm the crystalline phase identification.

3. Results and Discussion

The X-ray diffraction pattern obtained from the as-melt-spun ribbon is shown in Figure 1a and was indexed as a mixture of two oxides, cubic ZrO and a primitive big-cube phase. ZrO (JCPDS file number 00-020-0684) has a cubic unit cell with a = 4.62 Å and space group Fm-3m[18]. This cubic oxide is a metastable phase because not present in the Zr-O equilibrium diagram, but it is reportedly easily stabilized by impurities and/or surface effects[19]. The primitive big-cube phase (JCPDS file number 00-040-1035) also has a cubic unit cell with a =12.10 Å and a primitive but undefined space group[20]. This phase has been previously reported after crystallization of an oxygen-contaminated $Ni_{42}Zr_{58}$ melt-spun ribbon, where the presence of extra Bragg peaks suggested a lower symmetry crystal structure in comparison to the conventional big-cube which has the $E9_3$ crystal structure (space group Fd-3m)[20]. The observed Bragg peaks around 45º are superimposed on a broad amorphous diffraction band, indicating that small nanocrystals of the two phases have formed within the amorphous matrix upon cooling. Figure 1b shows the DSC thermogram of the alloy, obtained at a constant heating rate of 20 ºC/min. The curve is typical of an amorphous structure and exhibits two exothermic peaks characteristic of two crystallization processes. The onset crystallization temperature (T_x) is about 483 ºC with the second peak at ~525 °C. An endothermic peak characteristic of a glass transition (T_g) was not observed prior to the crystallization exotherms. These results are in accordance with the results reported by Déo et al.[12], who also did not observe the glass transition T_g in two similar compositions, $Zr_{26.8}Ni_{46.5}Cu_{26.7}$ and $Zr_{26.7}Ni_{44.8}Cu_{28.5}$ (at.%). Due to the higher heating rate used in the previous work (40 ºC/min), the onset crystallization temperatures (T_x) were slightly higher, 520 and 498 ºC, and with the second peaks for both at ~540 °C for those respective compositions. No attempts were made to characterize the crystalline phases associated with these exothermic peaks.

An SEM micrograph from the "air side" of the melt-spun ribbon is shown in Figure 2a, where the microstructure consists of an amorphous matrix containing a cluster of dendrites of the primitive big-cube phase, which indicates the probably nucleation and growth of the big-cube phase in the liquid prior to vitrification of the matrix. In contrast, the BSE image from a cross-section in Figure 2b revealed the presence of faceted crystals of the ZrO phase. The fraction of the ZrO phase on the cross section was estimated from image analysis to be ~4.3% and the average size was ~0.75 μm^2. The EDS results for the amorphous matrix and the crystalline phases are summarized in Table 1. While the measured amorphous matrix composition was similar to the nominal alloy composition, the faceted crystals in the cross-section view had a higher Zr content consistent with the ZrO identification, whereas the dendritic crystals observed on the ribbon surface contained a surprisingly low Zr concentration given that the expected stoichiometry of this phase was anticipated to be close to $Zr_4(Ni,Cu)_2O$[21].

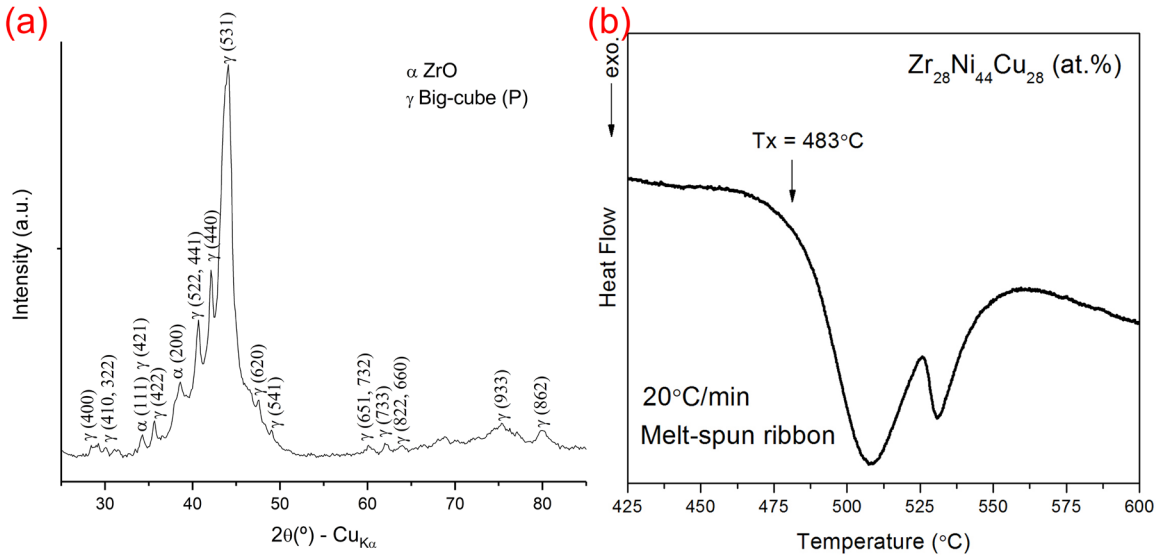

Figure 1. $Zr_{28}Ni_{44}Cu_{28}$ (at.%) melt-spun ribbon: (a) XRD pattern indexing the cubic phases ZrO and primitive big-cube, and (b) DSC curve indicating two crystallization peaks at ~483 and 525 °C.

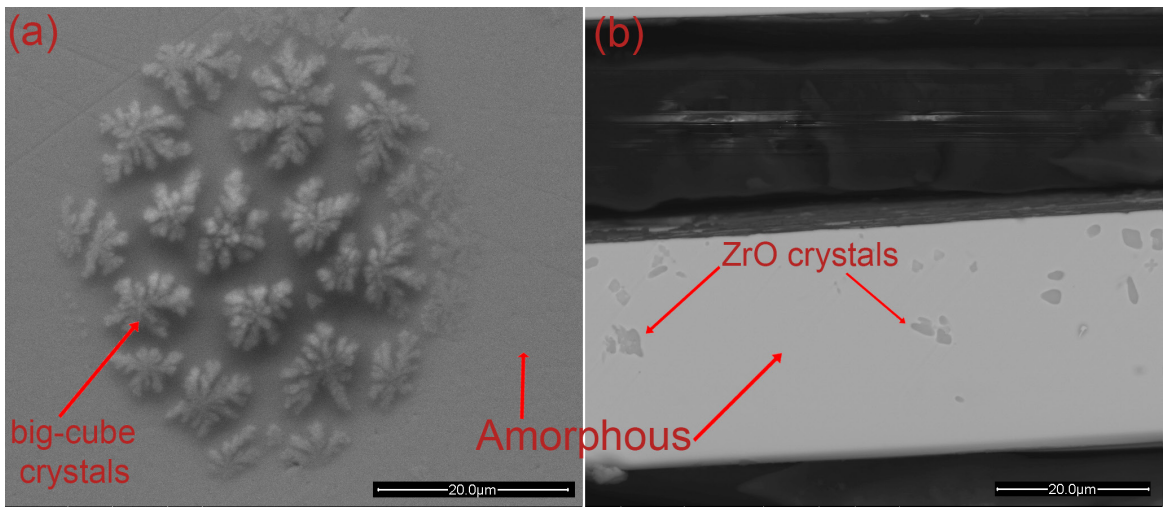

Figure 2. SEM images showing an amorphous matrix and some crystalline phases embedded in the ribbon (a) surface and (b) cross-section.

Table 1. Average compositions (at.%) of the amorphous matrix and the two different crystalline phases as measured by SEM-EDS. The O concentrations are only qualitative and for comparison given the low accuracy associated with quantification using EDS.

Region	Zr	Ni	Cu	O
Amorphous matrix	25.0	46.0	29.0	-
Big-cube dendritic crystals (surface)	18.3	25.0	15.3	41.4
ZrO faceted crystals (cross-section)	45.5	4.7	3.6	46.2

The bright-field TEM (BFTEM) image of the as-cast microstructure in Figure 3a reveals the amorphous matrix and one of the faceted crystals. The positions where the spot EDS measurements were taken are marked as “b” and “c”, and the EDS analysis of the amorphous matrix “b” indicated an approximate composition $Zr_{41.4}Ni_{35.2}Cu_{23.4}$, which is slightly Zr-rich relative to the nominal composition whereas the faceted crystal “c” exhibited mostly Zr and O, in agreement with the EDS measurements taken from the faceted crystals in the SEM that were believed to be the metastable ZrO phase. The SADP in Figure 3b taken from the amorphous matrix region “b” contains the expected diffuse rings. Two SADPs were taken from grain “c” along a <001> (Figure 3c) and a <112> (Figure 3d) zone axis and confirm the indexing of the FCC ZrO crystalline phase by XRD in Figure 1a. This is significant given that, to our knowledge, this phase has not been previously reported in similar rapidly-solidified alloys in this composition range.

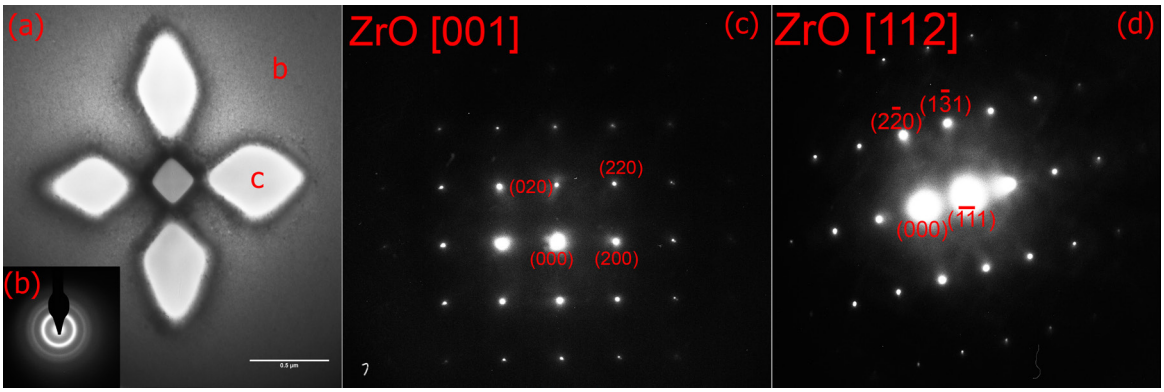

Figure 3. (a) BFTEM image of the amorphous matrix and faceted crystalline phase, (b) SADP from amorphous matrix "b", (c) [001] SADP from "c", and (d) [112] SADP from "c".

Liu et al. calculated a partial isothermal section of the Zr–Ni–Cu phase diagram at 800°C[22] and the investigated alloy composition falls into the predicted three-phase region where the $Cu_7Zr_3Ni_{10}$ ternary phase is in equilibrium with the $Cu_{51}Zr_{14}$ and $Cu_{10}Zr_7$ binary phases. Clearly, the experimental results are inconsistent with this phase diagram presumably due to a combination of the metastable nature of the processing and the oxygen contamination.

The present results indicate that the GFA of alloys containing large amounts of zirconium is compromised by the sensitivity of such alloys to oxygen contamination which is ubiquitous in Zr especially in thin melt-spun ribbons. One of the most common crystalline phases reported in rapidly-solidified Zr-containing alloys has been referred to as the "big-cube" phase which is an oxygen-stabilized FCC phase based on the Zr_4Ni_2O structure. This is sometimes referred to cubic Zr_2Ni given both the Zr:Ni ratio and the challenges in detecting oxygen due to its low fluorescent yield for characteristic x-rays[23].

Kaufman and Shull reported the formation of Ti_4Cu_2O (similar structure) as the first phase to form during annealing of glassy $Cu_{55}Ti_{45}$ melt-spun ribbons[24]. Mackay et al. concluded this family of oxides have the Fd-3m structure with a large unit cell[21] containing 96 metallic atoms with sites for 16 oxygen atoms if all sites are occupied (reason for the description "big-cube"). However, it is noted that lower O levels are common in this phase. Other more recent work has shown the presence of more than one "big-cube" Fd-3m oxide with distinct lattice parameters[25-27].

In addition, Altounian et al. proposed the formation of a Zr_4Ni_2O phase with all oxygen sites occupied based on the structure of Ti_4Ni_2O[20]. In addition, they also proposed that oxygen and zirconium, due their strong bonding, form clusters in the liquid that trigger crystallization of the "big-cube" phase as the first crystalline phase to form. Such Zr-O clusters in the liquid were proposed to have an octahedral configuration (oxygen atoms surrounded by six Zr atoms); however more recent analysis also indicate the possibility of a tetrahedral configuration[23]. Further, the easy substitution of different atoms, such as Ni and Cu in the $Zr_4(Cu,Ni)_2O$ phase also facilities its formation[23].

In general, we may assume that the formation of both characterized oxides, was facilitated by the larger negative value of mixing enthalpy between Zr and O vs. Zr-Cu, Zr-Ni, and Ni-Cu as well as other oxygen-metal pairs in the alloy. The mixing enthalpy is proportional to the interaction parameter, Ω, and the values for these atomic pairs are: −23 (Zr-Cu), −48 (Zr-Ni), 4 (Ni-Cu), and −1000 (Zr-O) (kJ/mol)[28,29]. The very negative value of Ω for the Zr-O atomic pair indicates that their bonding is extremely strong and consequently it is preferential compared to the other atomic pairs. In addition, the magnitude of Ω for Zr-O is much more negative than comparable parameters measured for oxygen with Ni and Cu[30]. The contribution of mixing enthalpy is quite large in stabilizing the ordered structures; hence the crystalline phases with more negative values of mixing enthalpy are thermodynamically more stable[31]. In the present system, the mixing enthalpy becomes more negative with increasing oxygen concentration and is consistent with the observation of zirconium oxide formation.

Oxygen levels of around 700 wppm in alloys with large amounts of zirconium can affect significantly the crystallization and the microstructures that develop in rapidly-quenched samples[32]. The crystallization of an undercooled alloy can be initiated by homogeneous nucleation of oxygen-containing compounds, such as ZrO and $Zr_4(Ni,Cu)_2O$[15]. In addition, the crystallization incubation time is strongly affected by the oxygen content since the oxides, or oxygen stabilized phases, can act as heterogeneous nucleation sites during the transition of liquid to solid[33]. The crystallization of oxides in the amorphous matrix can also change the shape of the crystallization peak during heating in a DSC experiment[12,34], even without changing significantly the characteristics of the temperatures and/or the thermal parameters in BMGs[34].

4. Conclusions

The two crystalline phases, cubic ZrO and a primitive "big-cube" $Zr_4(Ni,Cu)_2O$ phase, that form in $Zr_{28}Ni_{44}Cu_{28}$ melt-spun ribbons are both metastable and form in preference to the phases expected from the various binary diagrams or in the calculated partial ternary phase diagram for Zr-Ni-Cu. Their formation is consistent with an elevated oxygen concentration combined with rapid solidification and the

reported clustering of Zr and O in the liquid leading to ease of formation during solidification. Finally, the oxygen-induced crystallization observed in these ribbons is likely to occur in most alloys containing large amounts of zirconium (or titanium) with typical oxygen levels (below 1000 wppm) when solidified using rapid quenching techniques.

5. Acknowledgements

The authors would like to thank FAPESP process 2011/20690-6 for financial support and gratefully acknowledge the support by the Center for Advanced Non-Ferrous Structural Alloys (CANFSA) as well as the National Science Foundation Industry/University Cooperative Research Center (I/UCRC) [Award No.1624836] at the Colorado School of Mines. We appreciate Dr. F. G. Coury from DEMa-UFSCar (Brazil) for running the DSC experiment.

6. References

1. Sheng HW, Luo WK, Alamgir FM, Bai JM, Ma E. Atomic packing and short-to-medium-range order in metallic glasses. Nature. 2006;439:419-25. http://dx.doi.org/10.1038/nature04421.
2. Ashby MF, Greer AL. Metallic glasses as structural materials. Scr Mater. 2006;54:321-6. http://dx.doi.org/10.1016/j.scriptamat.2005.09.051.
3. Schuh CA, Hufnagel TC, Ramamurty U. Mechanical behavior of amorphous alloys. Acta Mater. 2007;55:4067-109. http://dx.doi.org/10.1016/j.actamat.2007.01.052.
4. Korkmaz S, Kariper A. Glass formation, production and superior properties of Zr-based thin film metallic glasses (TFMGs): a status review. J Non-Cryst Solids. 2020;527:119753. http://dx.doi.org/10.1016/j.jnoncrysol.2019.119753.
5. Basu J, Murty BS, Ranganathan S. Glass forming ability: Miedema approach to (Zr, Ti, Hf)-(Cu, Ni) binary and ternary alloys. J Alloys Compd. 2008;465:163-72. http://dx.doi.org/10.1016/j.jallcom.2007.10.131.
6. Mei-Bo T, De-Qian Z, Ming-Xiang P, Wei-Hua W. Binary Cu–Zr Bulk Metallic Glasses. Chin Phys Lett. 2004;21:901-3. http://dx.doi.org/10.1088/0256-307X/21/5/039.
7. Peng Q, Xie Y, Zhu B, Chen W, Schroers J, Chen M, et al. Joining mechanism of bulk metallic glasses in their supercooled liquid region. J Mater Process Technol. 2020;279:116583. http://dx.doi.org/10.1016/j.jmatprotec.2019.116583.
8. Ma X, Zhen N, Guo J, Li Q, Chang C, Sun Y. Preparation of Ni-based bulk metallic glasses with high corrosion resistance. J Non-Cryst Solids. 2016;443:91-6. http://dx.doi.org/10.1016/j.jnoncrysol.2016.04.020.
9. Lee MH, Lee JY, Bae DH, Kim WT, Sordelet DJ, Kim DH. A development of Ni-based alloys with enhanced plasticity. Intermetallics. 2004;12:1133-7. http://dx.doi.org/10.1016/j.intermet.2004.04.027.
10. Kawashima A, Sato T, Ohtsu N, Asami K. Characterization of surface of amorphous Ni-Nb-Ta-P alloys passivated in a 12 kmol/m^3 HCl solution. Mater Trans. 2004;45(1):131-6. http://dx.doi.org/10.2320/matertrans.45.131.
11. Chen LY, Hu HT, Zhang GQ, Jiang JZ. Catching the Ni-based ternary metallic glasses with critical diameter up to 3 mm in Ni–Nb–Zr system. J Alloys Compd. 2007;443:109-13. http://dx.doi.org/10.1016/j.jallcom.2007.02.114.
12. Déo LP, Mendes MAB, Costa AMS, Campos Neto ND, De Oliveira MF. Applying a new criterion to predict glass forming alloys in the Zr-Ni-Cu ternary system. J Alloys Compd. 2013;553:212-5. http://dx.doi.org/10.1016/j.jallcom.2012.11.123.
13. Lin XH, Johnson WL, Rhim WK. Effect of oxygen impurity on crystallization of an undercooled bulk glass forming Zr-Ti-Cu-Ni-Al alloy. Mater. Trans. JIM. 1997;38:473-7. http://dx.doi.org/10.2320/matertrans1989.38.473.
14. Błyskuna P, Maj P, Kozieł T, Pajor K, Kulik T. Zirconium purity influence on the critical diameter and thermal indicators of the Zr48Cu36Al9Ag7 alloy. J Non-Cryst Solids. 2019;509:80-7. http://dx.doi.org/10.1016/j.jnoncrysol.2019.01.026.
15. Gebert A, Eckert J, Schultz L. Effect of oxygen on phase formation and thermal stability of slowly cooled Zr65Al7.5Cu17.5Ni10 metallic glass. Acta Mater. 1998;46:5475-82. http://dx.doi.org/10.1016/S1359-6454(98)00187-6.
16. Gillen AG, Cantor B. Photocalorimetric cooling rate measurements on a Ni-5 wt% A1 alloy rapidly solidified by melt spinning. Acta Metall. 1985;33:1813-25. http://dx.doi.org/10.1016/0001-6160(85)90005-7.
17. Tkatch VI, Limanovskii AI, Denisenko SN, Rassolov SG. The effect of the melt-spinning processing parameters on the rate of cooling. Mater Sci Eng A. 2002;323:91-6. http://dx.doi.org/10.1016/S0921-5093(01)01346-6.
18. Khitrova VI, Klechkovskaya V. Electron-diffraction investigation of phase transformation and crystal structure of thin layers of cubic zirconium oxide. Kristallografiya. 1985;30:126-30.
19. Abriata JP, Garcés J, Versaci R. The O-Zr (Oxygen-Zirconium) system. Bull Alloy Phase Diagr. 1986;7:116-24. http://dx.doi.org/10.1007/BF02881546.
20. Altounian Z, Batalla E, Strom-Olsen J, Walter JJ. The influence of oxygen and other impurities on the crystallization of NiZr2 and related metallic glasses. J Appl Phys. 1987;61:149. http://dx.doi.org/10.1063/1.338847.
21. Mackay R, Miller GJ, Franzen HF. New oxides of the filled-Ti2Ni type structure. J Alloys Compd. 1994;204(1-2):109-18.
22. Liu CH, Chiang WR, Hsieh KC, Chang YA. Phase equilibrium in the Cu-Ni-Zr system at 800 °C. Intermetallics. 2006;14:1011-3. http://dx.doi.org/10.1016/j.intermet.2006.01.020.
23. de Oliveira MF, Kaufman MJ, Botta Filho WJ, Kiminami CS. The “Big-Cube” phase found in Zr-Cu-Al-Ni easy glass forming alloys. Journal of Metastable and Nanocrystalline Materials. 2002;14:101-6.
24. Kaufman MJ, Shull RD. Nature of Large Ti4Cu2O Particles Formed During Annealing of Cu55Ti45 Metallic Glass Ribbons. Metall Trans. 1986;17A:575-81.
25. Campos Neto ND, Pereira FS, Antonio SG, Guo Y, Clarke AJ, Kaufman MJ, et al. Phase formation maps in Zr48Cu46.5Al4Nb1.5 bulk metallic glass composites as a function of cooling rate and oxygen concentration. Mater Charact. 2019;158:109932. http://dx.doi.org/10.1016/j.matchar.2019.109932.
26. Teixeira CA, da Silva RV, Pereira LT, de Oliveira MF. Oxygen effect on bending behavior of a zirconium based bulk metallic glass. J Non-Cryst Solids. 2020;535(1):119966.
27. Campos ND No, Rocha RFCL, Pereira FS, Soares C, Santa Maria FH, Oliveira MF. Effective method to enhance the glass-forming ability of Vitreloy 105 containing high oxygen concentrations. Metall Mater Trans, A Phys Metall Mater Sci. 2020;51:3518-25. http://dx.doi.org/10.1007/s11661-020-05775-4.
28. Takeuchi A, Inoue A. Mixing enthalpy of liquid phase calculated by miedema’s scheme and approximated with sub-regular solution model for assessing forming ability of amorphous and glassy alloys. Intermetallics. 2010;18:1779-89. http://dx.doi.org/10.1016/J.INTERMET.2010.06.003.
29. Huang W. Oxygen solubility in Fe-Zr-O liquid. Calphad. 2004;28(2):153-7. http://dx.doi.org/10.1016/j.calphad.2004.07.007.
30. Wang W-E, Olander DR. Thermochemistry of the UO and ZrO Systems. J Am Ceram Soc. 1993;76:1242-8. http://dx.doi.org/10.1111/j.1151-2916.1993.tb03748.x.
31. Sriharitha R, Murty BS, Kottada RS. Phase formation in mechanically alloyed AlxCoCrCuFeNi (x = 0.45, 1, 2.5, 5 mol) high entropy alloys. Intermetallics. 2013;32:119-26. http://dx.doi.org/10.1016/j.intermet.2012.08.015.
32. He G, Bian Z, Chen GL. Structures and properties of a Zr-based bulk glass alloy after annealing. Mater Sci Eng A. 1999;270:291-8. http://dx.doi.org/10.1016/s0921-5093(99)00203-8.
33. Lin XH, Johnson WL, Rhim WK. Effect of oxygen impurity on crystallization of an undercooled bulk glass forming

ZrTiCuNiAl alloy. Mater Trans JIM. 1997;38:473-7. http://dx.doi.org/10.2320/matertrans1989.38.473.

34. Campos ND No, Soares C, Pereira FS, Bergamaschi V, Antonio SG, Kaufman MJ, et al. Glass forming ability and continuous-cooling-transformation (CCT) diagrams of Vitreloy 105 as function of cooling rate and oxygen concentration. J Non-Cryst Solids. 2020;528:119762. http://dx.doi.org/10.1016/j.jnoncrysol.2019.119762.